Gecko Adhesion on Flat and Rough Surfaces: Simulations with a Multi-Scale Molecular Model

Tobias Materzok,* Danna De Boer, Stanislav Gorb, and Florian Müller-Plathe

A multiscale modeling approach is used to develop a particle-based mesoscale gecko spatula model that is able to link atomistic simulations and mesoscale (0.44 µm) simulations. It is used to study the detachment of spatulae from flat as well as nanostructured surfaces. The spatula model is based on microscopical information about spatulae structure and on atomistic molecular simulation results. Target properties for the coarse-graining result from a united-atom model of gecko keratin in periodic boundary conditions (PBC), previously developed by the authors. Pull-off forces necessary to detach gecko keratin under 2D PBC parallel to the surface are previously overestimated when only a small region of a spatula is examined. It is shown here that this is due to the restricted geometry (i.e., missing peel-off mode) and not model parameters. The spatula model peels off when pulled away from a surface, both in the molecular picture of the pull-off process and in the force-extension curve of non-equilibrium simulations mimicking single-spatula detachment studied with atomic force microscopy equipment. The force field and spatula model can reproduce experimental pull-off forces. Inspired by experimental results, the underlying mechanism that causes pull-off forces to be at a minimum on surfaces of varying roughnesses is also investigated. A clear sigmoidal increase in the pull-off force of spatulae with surface roughness shows that adhesion is determined by the ratio between spatula pad area and the area between surface peaks. Experiments showed a correlation with root-mean-square roughness of the surface, but the results of this work indicate that this is not a causality but depends on the area accessible.

1. Introduction

The influence of surface roughness on the gecko adhesion has been previously studied on the nanoscale using atomic force microscopy (AFM) and on the macroscale in behavioral experiments with freely moving geckos.[1] Experimental data on the force necessary to pull off single spatulae from hard rough substrates and behavioral observations on living gecko clinging to various surfaces show that the effective adhesion experiences a minimum in root-mean-square roughness (RMS, R_q) from 100 to 300 nm.[1] This means that geckos can perform well on smooth substrates and those containing roughness values higher than the characteristic dimension of the terminal contact elements of the foot (so-called spatulae). Similar results on the geometrical relationships between spatula size, pull-off force and substrate roughness have been previously demonstrated for insects[2] and spiders[3] and supported by a relatively simple but elegant macroscale numerical model.[4]

At the end, gecko feet have thousands of mesoscale (≈0.1–0.5 µm) spatulae that allow geckos to stick to surfaces of varying chemistry, humidity,[5,6] and roughness.[1] Both experimental[1,7–13] and computational[5,6,14,15] researches have attempted to understand gecko adhesion mechanisms. While much remains to be learned, the present article offers a step forward in this field with the first molecular dynamics (MD) simulations of a multiscale model of a whole spatula in contact with surfaces at different roughness.

Our previous investigations of gecko adhesion using MD were done on the coarse-grained (CG) [5] and united-atom (UA)[6] level of molecular resolution. The model with the most detailed level of atomic resolution is UA, where apolar hydrogens are incorporated with their parent carbon atoms into single interaction sites (so-called "UAs"). With that model, we explained gecko adhesion in different scenarios (wet and dry, hydrophobic, and hydrophilic surfaces) on the molecular level. Our CG gecko keratin model treated entire amino acids of the amorphous region[16] as single bead and mapped the entire characteristic beta-sheet folding domain into another, larger single CG bead. With the CG model, we were able to

T. Materzok, D. De Boer, F. Müller-Plathe
Eduard-Zintl-Institut für Anorganische und Physikalische Chemie and Profile Area Thermofluids and Interfaces
Technische Universität Darmstadt
Alarich-Weiss-Str. 8, D-64287 Darmstadt, Germany
E-mail: t.materzok@theo.chemie.tu-darmstadt.de
S. Gorb
Zoological Institute Functional Morphology and Biomechanics
Kiel University
Am Botanischen Garten 1-9, D-24118 Kiel, Germany

The ORCID identification number(s) for the author(s) of this article can be found under https://doi.org/10.1002/smll.202201674.

understand the effect of water at the hydrophobic surface. Lastly, the mesoscale model of this work uses a coarse-graining procedure to map five whole gecko keratin molecules to a single bead to allow the simulation of a whole spatula. Since, in every coarse-graining step, we pass information from the more-detailed finer-grained model to the coarser model, the current mesoscale model is informed by the deepest level of atomic resolution currently available.

The initial main objective of this work was to investigate the relationship between the pull-off of a semi-infinite (periodic in one or more dimensions) spatula material (gecko keratin) flat-on-flat and the pull-off of a macroscopic spatula. Pull-off forces necessary to detach semi-infinite gecko keratin in 2D periodic boundary conditions (PBC) in MD were orders of magnitude larger than experimental pull-off forces of gecko spatulae when the adhesive spatula pad area is taken into account.[5,6] Our main hypothesis is that this discrepancy is not due to model parameterization. It is rather an artifact, which exists because periodic semi-infinite systems cannot describe the peeling-off process prevalent in the macroscopic detachment of gecko spatulae (and adhesive tapes).

Since MD simulations at the UA or CG scale cannot, with current computational power, simulate a whole gecko spatula, we chose to do a multiscale parameterization of a particle-based mesoscale gecko keratin model that reproduces pull-off pressure, Young's modulus, and Poisson's ratio of the UA reference model (GROMOS 54A7 force field[17–20]). We then applied the resulting force field of the mesoscale keratin material to describe an entire spatula. We use the MD software GROMACS[21] to allow direct comparison of both[5,6] other molecular simulations of gecko adhesion.

Besides the ability to make straightforward comparisons between the mesoscale model and the UA and CG models of gecko keratin, using MD instead of finite element method (FEM), where a meshed representation that follows constitutive laws defines material properties, has multiple advantages: i) the system's behavior comes naturally from particle interactions instead of constitutive laws; thus any process that we may not initially have thought about is allowed to happen naturally by attractive and repulsive forces; ii) constitutive laws do not need to be defined a priori, which could possibly miss critical processes or simplify things too much; iii) a spatula is still small enough to be a statistical-mechanical system and for entropic kinetic energy-related fluctuations to influence the behavior at interfaces. They are absent in FEM but have significant contributions in force probe molecular dynamics.[22]

2. Model Construction and Parameterization

2.1. Bulk Keratin Material Model

Gecko setae and spatulae are primarily made up of beta keratin proteins.[23,24] They form dimers and dimers accumulate to form fibrils.[16,23,25] The fibrils are thought to start at the proximal ends of setae and yield spatula at their distal ends.[25] In the setae, before branching off, the fibril regions are embedded in a soft matrix. After a seta branches into around one thousand individual spatulae, the matrix material decreases and

the spatulae are mostly made up of fibrillar regions with anisotropic elasticity.[16,25] We regard the gecko keratin material as a fiber-reinforced elastomer but do not explicitly model fibers and amorphous surroundings.[6] Instead, we use angle-dependent bond potentials between particles to model the anisotropic material characteristics of such a fiber-reinforced elastomer.

The fibrillar structure significantly contributes to mechanical properties, i.e., Young's Modulus E and Poisson's ratio v.[16] The spatula model must correctly describe the anisotropy arising from it. Our spatula model consists of very coarse-grained beads that incorporate about five keratin molecules. To this end, we introduce bead-bead harmonic bonds $V(r) = K / 2 \times (r - b_0)^2$ with an anisotropic bond force constant K and the equilibrium distance b_0. The anisotropic force constant becomes stronger as the direction of a bond aligns to the direction of the fibrils according to the equation:

$$K = k + k_b \times |\cos\theta| \tag{1}$$

where k is the isotropic part of the force constant assigned to every bond, k_b is an additional force constant in the fibril direction, and θ is the angle between the bond vector and the fibril direction. Hence, each bond in our model has an individual anisotropic bond constant depending on its angle towards the fibril direction in the initial structure. For the parameterization of k and k_b, see Section 2.4. Once assigned, the value of K remains unchanged.

To generate the basic periodic keratin model ("bulk keratin"), a box is randomly filled with beads at a number density of 0.012 nm^{-3} such that beads are a minimum of 2.8 nm apart from one another. The typical density of dry keratin $\rho = 1.3$ g cm^{-3} matches with the UA model of our previous work.[6] Using 1.3 g cm^{-3} as the target mass density, the bead number density of 0.012 nm^{-3} and the volume, the mapping scheme can be estimated: one bead accounts for 65 kD, a gecko keratin dimer for 22 kD; therefore our beads map the mass of five molecules (2.5 dimers). To model a highly cross-linked elastomer-like system similar[6,16] to gecko keratin, each bead is assigned harmonic bonds to its closest 30 neighboring beads. This connectivity is sufficient to make the real-scale spatula stiff enough and stop the system from collapsing. There is no excluded volume in the keratin-keratin interactions. For more than 10 bonds per bead, the system's volume remains essentially constant, with a volume drift of −30 nm^3 in a system of total size 21600 nm^3, see Figure S1A (Supporting Information).

The bond assignment algorithm does mean that some beads will have more than 30 bonds in total, depending on their environment. For each individual bond, we use the initial bead-bead distance as the equilibrium bond length b_0. This maintains the spatula shape when going from a quasi 0 K system to 300 K under the influence of an external potential (e.g., an attractive surface and a force detaching the spatula). The minimum system size required to prevent finite-size effects and to converge Young's modulus is a system of size $60 \times 60 \times 60$ nm^3 (Figure S1B, Supporting Information). For each simulation sample, a different bulk material configuration is generated randomly. Thus, all starting configurations are independent.

2.2. Spatula Model

The spatula model is created the same way as the bulk keratin model. The main difference is that the target volume into which beads are inserted is not a box but rather a realistic spatula shape. We used a scanning electron microscopy image from Xu et al.[26] and transferred the outline of the imaged spatula into a two-dimensional coordinate system. We cleaned up these coordinates since the image was not taken from an orthographic perspective and was not aligned to an optical axis. The resulting polygon is the outline in the x,y plane of a flattened spatula from a top-down perspective. Beads filled into this outline can be seen in **Figure 1** (Top) (the bond network is visible in Figure S2, Supporting Information). The polygon vertices are listed in Table S1 (Supporting Information). To generate different thicknesses in the z direction depending on the distance to the setae proximal end, i.e., distance to the spatula tip, we use two functions to follow the height of the spatula and insert beads only in between these two functions:

$$z_{\text{top}} = \left(\frac{z_h}{2} - r\right)/x_s \times x + r$$

$$z_{\text{bottom}} = \left(-\frac{z_h}{2} + r\right)/x_s \times x - r \tag{2}$$

with $z_h = 20$ nm the height of the spatula pad,[25] x_s the point between the shaft haft and the spatula pad, which is located at 65% the length of the spatula in x direction $l_x \times 0.65$ and $x = 0$ being located at the spatula haft face (extent and naming of different regions of the spatula can be found in Table S2, Supporting Information). The shaft haft side length in z and y is $r = 50$ nm (see Figure 1), a value comparable to the radius used in FEM models.[15,26] The (virtual) fibril direction goes from the shaft haft to the spatula pad tip, which is in the x direction in the initial setup. After bending (as described later), we generate the (virtual) fibrils again following the curvature, going from spatula haft to spatula pad tip by using a local orientation field
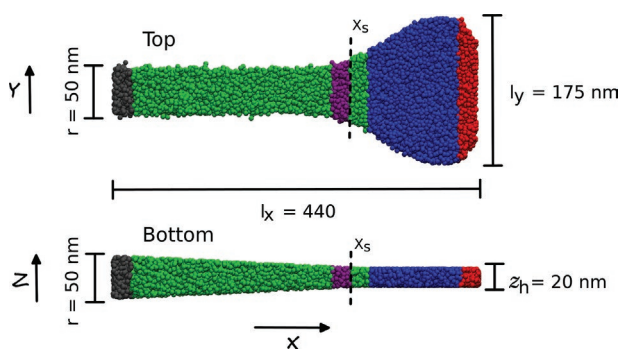
instead of the x direction. For each simulation sample, a new system is generated from scratch. In total, we simulate 10 spatulae, each having an independent starting configuration.

2.3. Surface Model

The surface is generated much like the bulk keratin model (Section 2.1). It has the same random arrangement of beads and the same bead density. For details, see Section S1 (Supporting Information). In total, we investigate eight peak densities ρ_{Peak} in which the total number of peaks per surface area ranges from 15.76 to 394.12 μm^{-2} (in addition to the perfectly flat surface with $\rho_{\text{Peak}} = 0$ μm^{-2}). In **Figure 2**, two such surfaces are shown.

We expect a surface representing an oxide mineral (e.g., the amorphous silica substrate of Huber et al.[8] that is used in the UA model of gecko keratin[6]) to not be able to deform. Such a surface is orders of magnitude stiffer than keratin, so we decided to make our surface completely rigid. Hence, we do not calculate interactions between surface beads and do not integrate the equation of motion for surface beads, effectively creating a space-fixed attractive external potential.

2.4. Parameterization of the Anisotropic Bonded Interactions of the Mesoscale Keratin Force Field

Experimental results have reported Young's moduli at a low of 1.2 GPa from nanoindentation tests and a high of 7.3 ± 1.0 GPa from in situ tensile tests.[27] Humidity also affects the elasticity of setal keratin, as 30% relative humidity produces $E = 3.2 \pm 0.2$ GPa and 80% relative humidity 2.2 ± 0.2 GPa.[28] A previous computational model found absolutely dry seta keratin to have a $E = 9.2$ GPa.[16] The target Young's modulus of 4.5 GPa for our spatula model is, thus, well within the range of experimental values and was set to reproduce the
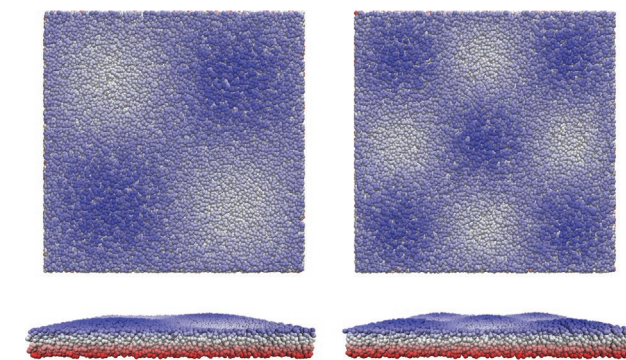

Figure 1. (Top) The top-viewing perspective of the spatula. The area of the spatula pad is $A_{\text{Sp}} = 19880$ nm^2. (Bottom) The shape of the spatula from its side is inspired by the finite element model of Sauer et al.[15] and the finite element calculations of Xu et al.[26] Keratin beads are colored in green, and we superimpose the green colored beads with named areas used throughout this work. Colors are illustrative and do not mean that properties differ between them. From left to right: spatula shaft haft (grey), joint (purple), and spatula pad (blue), which in this representation is overlaid by spatula tip (red). Table S2 (Supporting Information) summarizes these areas with the exact numerical values.

Figure 2. Two different surfaces are shown with increasing peak density (left $\rho_{\text{Peak}} = 15.76$ μm^{-2} and right $\rho_{\text{Peak}} = 39.41$ μm^{-2}). Beads are colored according to their height. For easier comprehension, the surfaces are not phase-shifted. In reality, depending on phase shift, the center of the surface (where the spatula attaches), could present anything between a valley and a peak. The height between the peak and valley is 16 nm for all surfaces, resulting in a root-mean-squared roughness of

$$R_q = \sqrt{\frac{1}{n}\sum(z_m - \langle z_m\rangle)} = 4 \text{ nm with } z_m \text{ the surface profile.}$$

**ADVANCED
SCIENCE NEWS**

www.advancedsciencenews.com

NANO · MICRO

small

www.small-journal.com

UA model of gecko keratin.[6] Existing literature on setae/spatulae keratin simply assumes a Poisson's ratio of $\nu = 0.2$,[15] 0.4,[16] or 0.5.[29] With our UA keratin model,[6] we calculated the Poisson's ratio to be $\nu = 0.4$ in the absolute dry state. Here, bond coefficients were tuned to yield $E = 4.5$ GPa and $\nu = 0.4$. The result of a wide range of combinations of k and k_b (Equation (2)) is shown in Figure S3 (Supporting Information), and details about the method are summarized in Section S2 (Supporting Information). The best fit to our UA target properties of $E = 4.5$ GPa and $\nu = 0.4$ is accomplished by $k_b = 1220$ kJ mol^{-1} nm^{-2} and $k = 226$ kJ mol^{-1} nm^{-2} (green symbol in Figure S3, Supporting Information), which results in $E = 4.518 \pm 0.036$ GPa and $\nu = 0.401 \pm 0.002$. Therefore, the mechanical properties of our model agree well with the above discussed experimental measurements.

2.5. Parameterization of the Nonbonded Interactions of the Mesoscale Keratin Force Field

We use force probe molecular dynamics (FPMD), as we have done in previous work.[5,6] We use FPMD to find the necessary size of the bulk keratin material for pull-off simulations and then to parameterize the nonbonded force field parameters for spatula-surface interactions. Details can be found in Section 3. The maximum force necessary to separate the bulk keratin system from the surface, called the pull-off force F_{pull}, is averaged over ten independently generated systems. To make the pull-off force intensive, we normalize it with the surface contact area, thereby calculating the pull-off pressures p.

With a mesoscale keratin material of height 20 and 90 nm box dimensions, the dimensions parallel to the surface (in Section S3 (Supporting information), we explain how we chose the box dimensions), the ε and σ values for a 12-6 Lennard–Jones (LJ) potential are parameterized against UA pulling results.[6] The UA model was, like the mesoscale keratin material used for the nonbonded parameterization, periodic in the directions parallel to the surface. For details about the UA model, see Section S4 (Supporting Information). Its force field was the GROMOS 54A7 FF.[17–20] It was made up of an amorphized gecko beta-keratin protein Ge-cprp-9, from which only the intrinsically disordered parts of the protein were considered. It was assumed that the disordered section of the protein is the part that is in contact with the surface and responsible for the adhesive interaction between spatula and surface.[6] The virtual cantilever is linked to the top half of the keratin in both the UA model and in the bulk keratin mesoscale model of this work, see **Figure 4** (red). We will come back to this in the computational details (Section 3).

At a loading rate of $\dot{F} = 1.66 \times 10^{12}$ pN s^{-1}, the average pull-off pressure of the UA model on top of a flat hydrophobic surface was $p = 12.92 \pm 5.3$ kJ mol^{-1} nm^{-3} (21.45 $\pm$ 8.85 pN nm^{-2}). Comparable pull-off pressures were found in previous coarse-grained work.[5] The hydrophobic surface model was a space-fixed flat surface of ≈ 3 nm height made up of GROMOS CH2 beads at a density of 20 nm^{-3}, which had a water contact angle of $\theta_c = 111.3°$.

This UA pulling pressure is the target against which we optimize the keratin-surface LJ parameters of the mesoscale

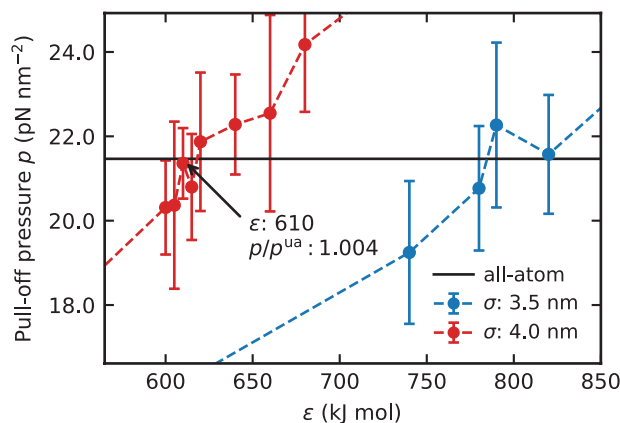**Figure 3.** Pull-off pressure as a function of Lennard–Jones (LJ) ε for the bulk keratin systems pulled off a hydrophobic surface with nonbonded LJ parameters σ at 3.5 nm (blue) or 4.0 nm (red). The periodic box dimensions are 90 nm $\times$ 90 nm and the force field parameters used for this validation are $k = 226$ kJ mol^{-1} nm^{-2} and $k_b = 1220$ kJ mol^{-1} nm^{-2}. The average is computed from 10 independent samples, and the standard deviation of the mean is used as the error.

model of this work, running pulling simulations for each parameter combination. The coarse-grained pull-off pressure are shown in **Figure 3**. For the production calculations, we use $\sigma = 4.0$ nm and $\varepsilon = 610$ kJ mol^{-1} for nonbonded interactions, which give the ratio of mesoscale and atomistic pull-off pressures $p/p^{ua} = 1.004$. Finally, we recall that nonbonded interactions exist only between the keratin and the surface. Interactions within the keratin are exclusively modeled as a network of harmonic bonds.

3. Computational Details

General simulation details can be found in Section S5 (Supporting Information), those concerning the mesoscale keratin material simulations (with PBC) are summarized in Section S5.1 and Section S5.2 (Supporting Information).

The mesoscale spatula is prepared in six steps; for details, see Section S6 (Supporting Information). After the first 4 steps, the final preparation, which involves pulling, is broken into two parts, as was done[15] by Sauer et al. The spatula shaft is first
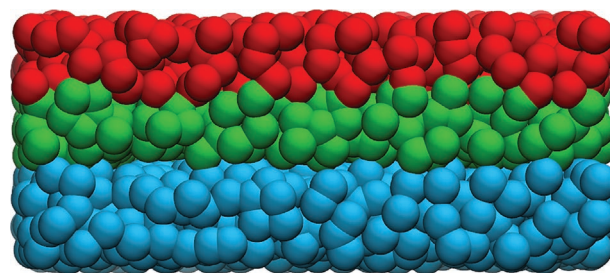

Figure 4. The mesoscale keratin material (green) used in the non-bonded parameterization on top of a flat surface (cyan) of dimensions 90 nm $\times$ 90 nm. The system is periodic in the two dimensions parallel to the surface. The surface height is 13 nm and the bulk material is 20 nm thick. Highlighted in red is the top-half of the bulk keratin. The center-of-mass of the top-half is connected to a virtual cantilever.

**ADVANCED
SCIENCE NEWS**
www.advancedsciencenews.com

NANO · MICRO
small
www.small-journal.com

bent upwards so that it has an inclination of some degree to the surface (step 5), equilibrated at this point. Then the equilibrated spatula configuration is pulled vertically at the shaft haft off the surface (step 6).

Equilibrium configurations are extracted from the trajectory at spatula inclinations of θ_S = 45, 60, and 75°, as shown in **Figure 5**, which are the same configurations as examined by Sauer et al.[15] The spatula inclination θ_S is the angle between the vector pointing from the joint to the shaft haft and the vector parallel to the surface, with the joint being at $l_x \times 0.35$ to $l_x \times 0.4$, as shown in Figure 1B in purple.

Although it is unknown what exact spatula inclination exists in nature, some inclination can be assumed from experimental imaging,[35–37] so we reset the bond network of the extracted configurations and regenerate all anisotropic bonds using the local fibril direction. The local fibril direction is calculated with a spline fit through the averaged positions of beads in the plane dissecting the spatula and normal to the surface. In essence, a local orientation field is used to calculate the bond angle, with the center between two connected beads as the bond position. Reapplying the bond assignment algorithm changes the equilibrium shape of the spatula to that of the target inclination. These shapes at θ_S = 45°, 60°, and 75° are the final equilibrium configurations of the spatulae that are used in the pull-off simulations, similar to the previous investigation by Sauer et al.[15]

For calculations involving a rough surface, the inclined spatulae (only θ_S = 45° is used) are placed on top of a surface with different peak densities. In the preload step (an applied external pressure of 0.2553 kJ mol^{-1} nm^{-3} or 0.4 pN nm^{-2}, corresponding to a force of 5076 kJ mol^{-1} nm^{-1} in case of the full-size spatula, we remember the spatula pad area is A_{Sp} = 19880 nm^2) is applied for 600 ns. Subsequently, the system is relaxed for 500 ns with no applied force. These are times sufficient to converge the distance between spatula and surface completely.

In the final pull-off simulation, the spatula is pulled away from the surface by linking the center of mass of the spatula shaft haft (Figure 1, grey) to a virtual cantilever (with the harmonic force constant k_{pull} = 1000 kJ mol^{-1} nm^{-2}) and moving the virtual cantilever at a constant pulling velocity away from the surface. The pulling velocities of the cantilever result in loading rates $\dot{F}$ = 16.6 × 10^{12} pN s^{-1}, 1.66 × 10^{12} pN s^{-1}, 0.83 × 10^{12} pN s^{-1} and 0.332 × 10^{12} pN s^{-1}.

To summarize all steps of the entire spatula pull-off process and simulation: i) generate the spatula and create bonds; ii) preload the spatula pad against the flat surface; iii) relax the

system; iv) move the spatula shaft haft COM 20 nm upwards; v) bend the spatula upwards by applying force normal to the shaft; vi) extract configurations with defined spatula inclinations and recreate the bond network; vii) pull the spatula vertically off the surface by the shaft haft COM.

Additionally, we simulate spatula detachment from rough surfaces using the resulting spatula configuration from step (vi). To summarize the simulations involving a rough surface: (viii) preload the spatula for 600 ns against the rough surface; (ix) relax the system; (x) pull the spatula off the rough surface.

There are effectively no periodic boundary conditions. The static surface has an area of 356 × 356 nm^2. The surface and spatula are surrounded by vacuum. All spatula detachment simulations are done in the NVT ensemble with a thermostat keeping the temperature constant at 300 K. As for the detachment simulation of periodic mesoscale keratin material, the preload step uses a SD thermostat[34] with τ_T = 1 ps; the relaxation step uses SD with τ_T = 10 ps; and all other steps use a velocity rescaling thermostat[33] with τ_T = 1 ps.

4. Results and Discussion

4.1. Spatula Detachment with Varying Loading Rates at 45° Inclination

By comparing the pull force against the time of periodic mesoscale keratin material in **Figure 6**A to the spatula pull-off (Figure 6B) (with milestones denoted by vertical lines and the corresponding times), it is clear that the pull-off proceeds differently. In the case of the periodic material, the force (here shown as pressure) increases linearly with time until a maximum is reached. This pull-off force (also called critical force or rupture force) is then overcome, and the material detaches quickly, as can be seen in the displacement of the center of mass of the top-half of the keratin-sheet (red). For the spatula (Figure 6B), the force does not increase linearly but changes in slope. At the peak of the force curve (139–156 ns for a loading rate of 1.66 × 10^{12} pN s^{-1}), the maximum is not sharply defined but stretches over a time period (and displacement range). This behavior is only seen with the spatula shape because the spatula pad is peeled-off by delamination (see **Figure 7** 139–156 ns). After reaching the critical force needed to detach the spatula from the surface, the force oscillates around zero (at $t > 160$ ns). However, the oscillation is less distinctly harmonic
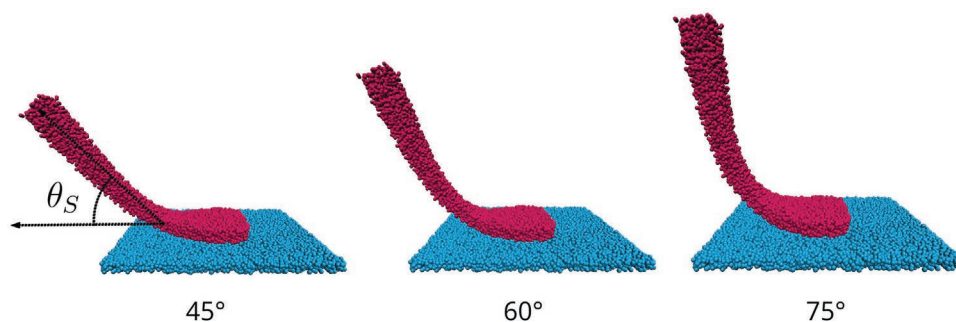

Figure 5. Equilibrium configurations of spatulae at different inclinations. The spatula inclination θ_S is defined as the angle between spatula shaft haft, joint and surface, as illustrated in the figure with black vectors.

ADVANCED
SCIENCE NEWS
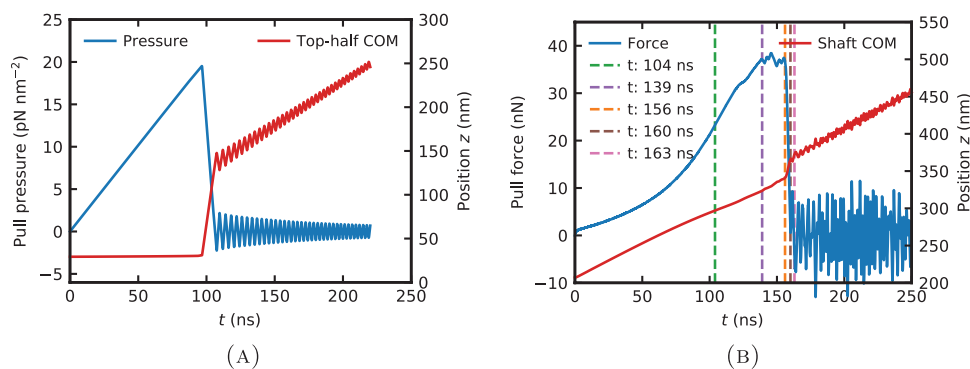www.advancedsciencenews.com

NANO · MICRO
small
www.small-journal.com

Figure 6. A) Pull-off of the bulk keratin material from a flat surface at a loading rate of $\dot{F} = 1.66 \times 10^{12}$ pN s^{-1}. The pull-off pressure is shown in blue, and the displacement of the shaft position is shown in red, with "Top-half COM" denoting the center of mass (COM) of the top half of the bulk keratin and "Shaft COM" the COM of the shaft haft. After detachment (around $t = 100$ ns), the material is quickly pulled up (red) away from the surface and oscillates around the virtual cantilever (red line oscillations at $t > 100$ ns), resulting in oscillations in the force. B) Pull-off force of a spatula (inclination $\theta_S = 45°$) from a fixed flat surface at a loading rate of 1.66×10^{12} pN s^{-1}. For illustrative purposes, one single trajectory is shown ($n = 1$).

compared to the periodic mesoscale keratin material since the spatula geometry allows other motions (e.g., wiggling) in addition to vertical oscillations of its center of mass (See Movie S1, Supporting Information).

The pull-off force and pull-off pressure (i.e., their respective maximum values) have been observed to be proportional to the logarithm of the loading rate,[38] as $F_{pull} \sim \log(\dot{F})$. To investigate this dependence in more detail in our work, **Figure 8**A shows the dynamic force spectrum where each data point is the average over 10 independent spatula systems. At the lowest loading rate, the pull-off force needed to detach the spatula from the surface is ≈35 nN. This value increases with the loading rate. At $\dot{F} = 16.6 \times 10^{12}$ pN s^{-1}, it reaches 60 nN. Loading rates in the order of 10^{12} pN s^{-1} are not accessible by experiments, with the fastest atomic force microscopy (AFM) experimental loading rates[39] only reaching orders of 10^8 pN s^{-1}.

With a smaller spatula that consists of fewer beads, lower loading rates are computationally accessible. We, therefore, scale down the mesoscale spatula to 70% of its original size to reduce the number of particles and allow longer simulation times. To give an idea about trends at lower loading rates, in Figure 8B, the pull-off pressure p of our full-size spatula model is displayed together with that for a smaller spatula. It shows a systematic difference between different sized spatulae. This difference exists not only for the pull-off pressure p (round markers) but also in the position of the maximum force as a function of the loading rate (triangle markers). It may be a result of the fact that the amount of material involved in bending is smaller with a smaller spatula, and the curvature to accomplish the same inclination, larger, thereby creating a stiffer spatula. This stiffer spatula has a smaller change in the

position of the maximum force. Smaller spatulae also have the additional benefit of allowing more adhesive contacts by setal area,[40] which was clearly exploited by evolution since animal groups with heavier representatives (lizards) use more but smaller pads.[36]

Both pull-off pressure and the change in the position of maximum force show that there are two regimes: one at lower loading rates that seems to be scaling linearly with $\log(\dot{F})$, and a change in the slope with the highest loading rate. If we assume the linear-log law for pull-off force against loading rate to continue down to experimental loading rates, we can extrapolate the pull-off force F (Figure 8B). The extrapolated pull-off force $F_{predicted} = \log(\dot{F} \times m) \times F_0$ for a spatula in the AFM-accessible regime is 25 nN for $\dot{F} = 10^8$ pN s^{-1} and 12 nN for $\dot{F} = 10^4$ pN s^{-1}. These pull-off forces match very well with pull-off forces of spatulae from experiments, which were found to be in the range of 8–20 nN.[1,8,9] It should be noted, however, that loading rates are not given in the literature, so we can only presume that they are somewhere between 10^1 and 10^8 pN s^{-1}.

Since the pull-off forces match well with experiments, this validates the spatula model created in this work. This validation, in itself, is a major result of the current work, as there is no other work that reproduces experimental gecko spatula pull-off forces in a bottom-up fashion.

4.2. Energy Contributions to Spatula Detachment

The rupture of the adhesive interactions between the spatula and the surfaces during pull-off involves the dissipation of adhesive and bending energy, with the dissipated adhesive energy
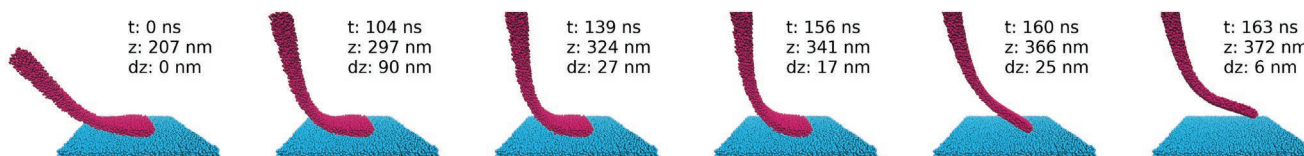

Figure 7. Process of pulling of a spatula ($\theta_S = 45°$) from a flat surface. In the first few hundred nanoseconds, the spatula bends as the spatula shaft is pulled upwards, normal to the surface. Between 140 ns and 160 ns, the spatula pad is peeled off the surface. As the crack moves from the spatula joint to the spatula tip, the adhesion energy is overcome and the detachment of the spatula pad occurs quickly in under 3 ns. After detachment, the energy stored in the spatula material from bending is released into a wiggling motion that may lead to short re-attachments of the spatula.
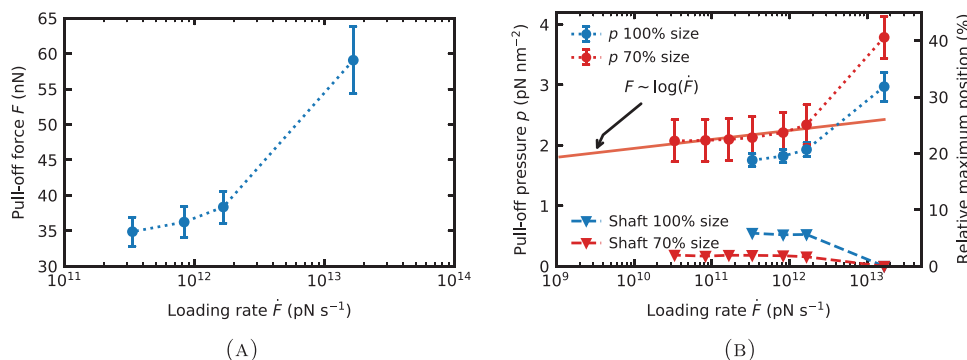
Figure 8. A) Dynamic force spectrum of spatula ($\theta_S = 45°$) pull-off against loading rate at a flat surface. B) Dynamic pressure spectrum shows the pull-off forces normalized with the area under the spatula pad. Here, the differently sized spatulae are compared. Since the smaller spatula includes fewer beads, lower loading rates are computationally more accessible. The pull-off pressure p (left axis) and the percentage change of the position of maximum force z_{COM}^f of the spatula shaft compared to a reference position at fastest pulling $z_{COM}^f(\dot{F} = 16.6 \times 10^{12} \text{ pN s}^{-1})$ (right axis) are shown against the loading rate. Round markers denote the pull-off pressure and triangle markers are used for the change in maximum position due to loading rate. The relative maximum position is defined as the shift of the position of the force maximum at the given loading rate $z_{COM}^f(\dot{F})$ with respect to that at the maximum loading rate $16.6 \times 10^{12} \text{ pN s}^{-1}$ in percent. The average is computed from 10 independent samples, and the standard deviation of the mean is used as the error.

$|\Delta U_{LJ}|$ being generally smaller than the work required to break adhesive interactions.[41] We calculate $|\Delta U_{LJ}|$ as the sum of the change of the nonbonded interactions between spatula and surface. We calculate the pull-off work as $\Delta W_P = -\int F_{pull} \, dz_{COM}$, with z_{COM} denoting the position of the shaft haft COM (see Figure 1). We compute the ratio $|\Delta U_{LJ}|/\Delta W_P$ for four different loading rates averaged over 10 independent simulations as a function of z_{COM} (In Figure S5A (Supporting Information), the ratios at the position of maximum force are highlighted in red; in Figure S5B (Supporting Information), the properties are shown side-by-side) and summarized in **Figure 9** for all contributions. Depending on the loading rate, ≈54–66% of the pull-off work is the cost of overcoming the adhesive interactions between spatula and surface. Only in the case of a very high loading rate of $16.61 \times 10^{12} \text{ pN s}^{-1}$ (blue) is the cost of overcoming adhesive interactions significantly lower at ≈30%. A related computational investigation of the adhesive behavior of amyloid nanofibers showed a cost of 80% in a pure peeling

situation and ≈50–60% for a situation where a joint, or hinge, was present.[42]

The ratio between bending energy $|\Delta U_{Bond}|$ and pull-off work W_p (Figure 9 and as a function of distance shown in Figure S5C and the underlying energies in Figure S5D, Supporting Information) shows a smaller contribution of ≈7–29%. In the case of the fast pull-off, the bending energy accounts only for 7% of the work needed to overcome attachment. At the slowest loading rate, the work needed to overcome the bending of the spatula is 29% of the total work needed.

At high loading rates, energy is dissipated as heat ("Rest"). This rest is dissipated into kinetic energy and can be measured as a temperature increase of the spatula in the NVE ensemble (when no thermostat regulates the temperature).

Until the position of maximum force, the bending energy $|\Delta U_{Bond}|$ increases and opposes the process as the spatula stretches and bends upwards out of its equilibrium inclination.

Force response on loading rate has been investigated on various levels,[38,43,44] and it is known that pulling too quickly leads to biased attached-to-detached pathways.[44] We show here that this trend is also true for pulling a spatula off a surface.
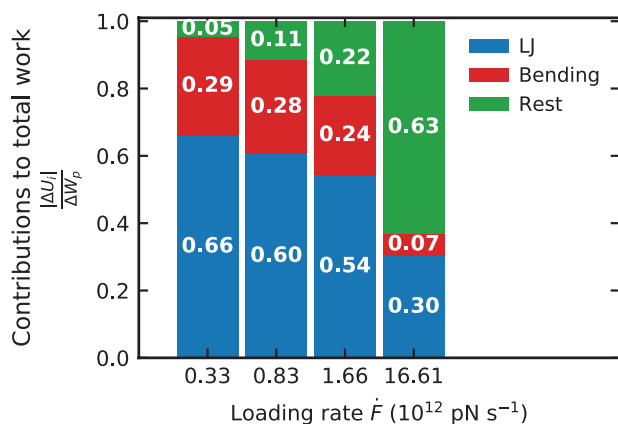
4.3. Spatula Detachment for Different Spatula Inclinations

A highly curved spatula has a higher pull-off force (**Figure 10**) than a less curved spatula. Our results show the opposite trend of what Sauer et al. produced with their FEM model.[15] They showed that as the spatula curvature increased, the pull-off force decreased. They assume that spatulae are straight, whereas we assume that spatulae have some inherent curvature. These authors' assumption implies that bending energy favors the detachment because the straight spatula is bent upward during pull-off, and the potential energy increases with the upward bending of the spatula. The contribution of the bending energy $|\Delta U_{Bond}|$ to the work of pull-off $W_p = \Delta U_{LJ} + \Delta U_{Bond} + \Delta U_{rest}$ would be negative and would compensate, in part, the spatula pad adhesion. Thus, the more the spatula is curved, the
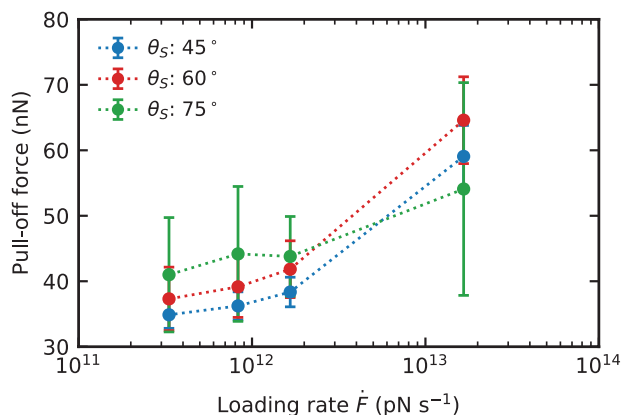

Figure 9. The ratio of overcome adhesive energy (blue) at the position of the maximum force is compared to overcome contributions from bending (red) and dissipated rest (green) energies to work of pull-off for different loading rates (for $\theta_S = 45°$). The ratios are annotated at the stacked bars. The average is computed from 10 independent samples.

**ADVANCED
SCIENCE NEWS**

www.advancedsciencenews.com

**NANO · MICRO
small**

www.small-journal.com

Figure 10. Dynamic force spectrum of spatula pull-off against loading rate depends on spatula inclination θ_S. Shown is the force spectrum for a perfectly flat surface. We assume that the average pull-off force for $\theta_S = 75°$ at the highest loading rate (green) is influenced by the large error, and its position below the two other θ_S pull-off force should not be taken as a true trend. The average is computed from 10 independent samples, and the standard deviation of the mean is used as the error.

stronger the pad adhesion would be compensated, resulting in smaller pull-off forces for highly curved spatulae. However, we observe something different, a highly curved spatula has a higher pull-off force (Figure 10) as the bending energy is smaller (Figure S6, Supporting Information), and the compensation is, thus, necessarily smaller in these geometries. This observation is confirmed by the contributions from the adhesive and bending, and dissipated energies overcome (Figure S6, Supporting Information).

With increasing spatula inclination θ_S, the error in the pull-off force F increases at all loading rates (Figure 10). A spatula inclination of 45° has the lowest pull-off force and the most minor error. As the curvature of the equilibrium spatula shape increases, the pull-off force and standard deviation increase, too.
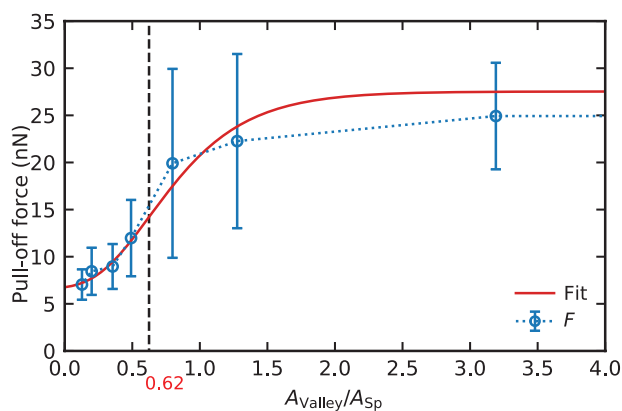

Figure 11. Pull-off force as a function of A_{valley}/A_{Sp}. The pull-off forces averaged over 10 independent simulations (blue) are used to fit a sigmoidal (Richards[45]) curve (red) that is used to compute the second derivative of this fit (not shown). The intersection of the second derivative of the sigmoidal curve with zero at $A_{valley}/A_{Sp} = 0.62$ is marked with a vertical black line. The average is computed from 10 independent samples, and the standard deviation of the mean is used as the error.

This last point is essential since different AFM-based studies of gecko adhesion may differ in the angle of connecting the spatula to the cantilever. There could be further implications if different geckos have different spatula inclinations or if variability in spatula inclinations between spatulae of the same seta exist.

Returning to Sauer et al., the contrast between our and their results might also stem from the differences in their FEM treatment compared to our MD treatment of the pull-off. In non-equilibrium MD, we simulate an AFM-like pull-off. However, the FEM study does not consider dynamics, loading rates or any lost dissipated "rest" energy and essentially treats pull-off at equilibrium.

4.4. Influence of Surface Roughness on Spatula Adhesion

Spatula adhesion has been observed to depend on surface RMS roughness, R_q[1,35] (the RMS distance between the surface profile and its average height). Huber et al.[1] demonstrated that as a surface changes from low R_q to high R_q, the pull-off force passes through a wide minimum between $R_q = 100$ nm and 300 nm. The authors hypothesized that when R_q is on the scale of spatula sizes, it allows only partial contact between the spatula and the surface because the asperities (the peaks and valley) would be too small for the spatula to attach to.

In **Figure 11**, the spatula pull-off force against the area per valley ratio $A_{valley} = 1/\rho_{peak}$ to spatula area A_{Sp} (top) at constant $R_q = 4$ nm, is shown (Figure S7 (Supporting Information) shows the pull-off force against the peak density)and summarized, as the peak density decreases, the pull-off force increases. The ratio A_{valley}/A_{Sp} is well fitted by a sigmoidal (Richards[45]) curve fit (red). When the spatula area exceeds the area of surface asperities ($A_{valley}/A_{Sp} < 1$), the spatula is unable to form close contact with the surface (**Figure 12**). The assumption of Huber et al.[1] that spatulae cannot adhere to asperities of similar but smaller dimensions is confirmed here. However, this is not necessarily a function of the RMS roughness. Their surfaces were fortuitously crafted with different roughness wavelengths that also resulted in different RMS roughnesses. Our results indicate a primary dependence on roughness wavelength rather than RMS roughness R_q.

Movie S2 (Supporting Information) shows the pull-off at $A_{valley}/A_{Sp} = 3.19$. At $A_{valley}/A_{Sp} < 1$; the pull-off force declines rapidly until the spatula cannot follow the surface topography anymore and simply attaches to the peaks of the surface, as seen in Figure 12 at $A_{valley}/A_{Sp} < 0.49$. A critical trend change can be observed when the area per valley reaches a value of $\approx 60\%$ (Figure 11) of the spatula pad. Asperities with smaller sizes prohibit the spatula from completely attaching to the surface (Figure 12).

There is a small apparent discrepancy between the pull-off force for the flat surface in Figure 11 (28 nN) and that of the loading rate investigations (Figure 8, 37 nN). This is due to the different preparation of the systems (no preloading in Figure 8). The minimum pull-off force ≈ 7 nN, is seen at a peak density of $A_{valley}/A_{Sp} = 0.13$. Movies S3, S4, and S5 (Supporting Information) display multiple starting configurations where the spatula is attached to surfaces of $A_{valley}/A_{Sp} = 3.19$, 1.28, and 0.49.
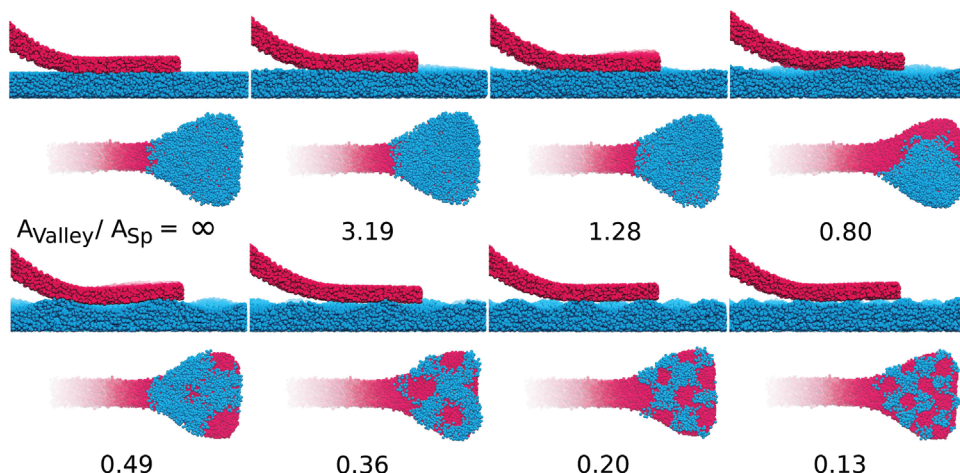
ADVANCED
SCIENCE NEWS
www.advancedsciencenews.com

NANO · MICRO
small
www.small-journal.com

Figure 12. (Top) Sections of spatula attached to rough surfaces shown with increasing peak density (from top left with $\rho_{Peak} = 0$ μm^{-2} to bottom right with 394.12 μm^{-2}). The average height between the peak and valley is 16 nm for all surfaces, resulting in a root-mean-squared roughness of $R_q = 4$ nm. (Bottom) Viewed from underneath the surface, the only part of the spatula displayed are surface beads (cyan), which are inside the interaction cutoff of the spatula beads (red). The ratio A_{valley}/A_{Sp} between the area between peaks and the spatula area is noted underneath each surface.

5. Conclusion

We developed a mesoscale particle model for a gecko spatula to study the effect of sub-micron surface roughness on the spatula adhesion. The model whose building blocks have the size of 65 kDa or 83 nm^3 has been constructed using the results from finer-grained molecular models, namely atomistic and coarse-grained (one bead per amino acid).

We thus bridge the nanoscale atomistic molecular simulations of keratin-surface interaction to mesoscale simulations of whole spatulae. Using a hybrid bottom-up-top-down coarse-graining protocol, we showed successfully that the UA model of gecko keratin[6] provides the correct adhesive interactions with the surface. Naive extrapolation of vertical pull-off simulations in 2D PBC of gecko keratin to sizes of real spatula pads greatly overestimated the force necessary to detach the spatula since pull-off forces would be hundreds of times larger than what AFM experiments showed. Here we showed that the CG force field parameterized in 2D PBC, which reproduces the UA keratin properties, matches with AFM studies if the same force field is used for a mesoscale spatula with its true shape and size. Using a simple extrapolation from fast MD loading rates to likely AFM loading rates, we observe typical pull-off forces for single spatulae of ≈12 nN (exp. 8 to 20 nN[1,8,9]). The necessary ingredient is to use the actual shape of a spatula and allow peel-off, rather than vertical detachment, to happen.

Spatulae of various sizes show systematic differences in pull-off. Per contact area, the pull-off force of a smaller spatula is larger. Using the same amount of material, more and smaller spatulae are therefore more "efficient". We find that it is the higher stiffness of smaller spatulae that oppose the peel-off.

Analysis of the energy contributions to spatula pull-off showed that around two-thirds of the pulling work is expended to overcome the adhesive nonbonded interactions, around one-third is the energy to bend the spatula, and only ≈5% is lost through dissipation (at the lowest loading rate). The partitioning of energies is, of course, model-dependent. It is, however, unlikely that the contributions of the adhesive interactions

will change much since our mesoscale coarse-graining is based on the result of UA adhesive interactions. When the maximum force is reached, and the spatula is about to be detached, the force is essentially only determined by adhesive nonbonded interactions.

Care should be taken in AFM experiments to correctly characterize the spatula since the adhesion also depends on the inclination of the spatula θ_S, and as inclination increases, its error increases too. High inclinations increase the pull-off force due to smaller compensation of the pad adhesion during bending. Large scatter of pull-off forces due to high inclinations of $\theta > 60°$ may also lead to premature detachments of spatulae or parts of synthetic gecko adhesives, which would decrease the product's overall reliability.

The spatula pull-off force shows a strong dependence on the characteristic wavelength of the surface roughness, i.e., the lateral extent of depressions and protrusions. The pull-off force follows a sigmoidal increase. At short wavelengths, the spatula cannot follow the terrain and, in turn, can only attach to the peaks of the rough surface. The most significant increase of pull-off force happens where the area per surface feature reaches about 60% of the area of the spatula pad. From this point on, the spatula can closely attach to the surface topography.

Supporting Information

Supporting Information is available from the Wiley Online Library or from the author.

Acknowledgements

Conflict of Interest

The authors declare no conflict of interest.

Data Availability Statement

The data that support the findings of this study are available from the corresponding author upon reasonable request.

[1] G. Huber, S. N. Gorb, N. Hosoda, R. Spolenak, E. Arzt, *Acta Biomater.* **2007**, *3*, 607.
[2] D. Voigt, J. M. Schuppert, S. Dattinger, S. N. Gorb, *J. Insect Physiol.* **2008**, *54*, 765.
[3] J. O. Wolff, S. N. Gorb, *J. Exp. Biol.* **2012**, *215*, 179.
[4] A. Kovalev, A. E. Filippov, S. N. Gorb, *Bioinspir. Biomim.* **2018**, *13*, 066004.
[5] T. Materzok, S. Gorb, F. Müller-Plathe, *Soft Matter* **2022**, *18*, 1247.
[6] T. Materzok, A. Canestraight, S. N. Gorb, F. Müller-Plathe, **2022**, in preparation.
[7] K. Autumn, Y. A. Liang, S. T. Hsieh, W. Zesch, W. P. Chan, T. W. Kenny, R. Fearing, R. J. Full, *Nature* **2000**, *405*, 681.
[8] G. Huber, H. Mantz, R. Spolenak, K. Mecke, K. Jacobs, S. N. Gorb, E. Arzt, *Proc. Natl. Acad. Sci. U.S.A.* **2005**, *102*, 16293.
[9] W. Sun, P. Neuzil, T. S. Kustandi, S. Oh, V. D. Samper, *Biophys. J.* **2005**, *89*, L14.
[10] K. Autumn, S. T. Hsieh, D. M. Dudek, J. Chen, C. Chitaphan, R. J. Full, *J. Exp. Biol.* **2006**, *209*, 260.
[11] H. Izadi, K. M. E. Stewart, A. Penlidis, *J. R. Soc. Interface* **2014**, *11*, 20140371.
[12] A. Y. Stark, M. R. Klittich, M. Sitti, P. H. Niewiarowski, A. Dhinojwala, *Sci. Rep.* **2016**, *6*, 30936.
[13] A. Y. Stark, S. Subarajan, D. Jain, P. H. Niewiarowski, A. Dhinojwala, *Philos. Trans. Royal Soc.* **2016**, *374*, 20160184.
[14] R. A. Sauer, *Comput. Methods Biomech. Biomed. Eng.* **2009**, *12*, 627.
[15] R. A. Sauer, M. Holl, *Comput. Methods Biomech. Biomed. Eng.* **2013**, *16*, 577.
[16] K. S. Endoh, T. Kawakatsu, F. Müller-Plathe, *J. Phys. Chem. B* **2018**, *122*, 2203.
[17] L. D. Schuler, X. Daura, W. F. V. Gunsteren, *J. Comput. Chem.* **2001**, *22*, 1205.
[18] C. Oostenbrink, A. Villa, A. E. Mark, W. F. V. Gunsteren, *J. Comput. Chem.* **2004**, *25*, 1656.
[19] N. Schmid, A. P. Eichenberger, A. Choutko, S. Riniker, M. Winger, A. E. Mark, W. F. van Gunsteren, *Eur. Biophys. J.* **2011**, *40*, 843.
[20] W. Huang, Z. Lin, W. F. van Gunsteren, *J. Chem. Theory Comput.* **2011**, *7*, 1237.
[21] B. Hess, C. Kutzner, D. van der Spoel, E. Lindahl, *J. Chem. Theory Comput.* **2008**, *4*, 435.
[22] B. Heymann, H. Grubmüller, *Biophys. J.* **2001**, *81*, 1295.
[23] D. L. Hallahan, N. M. Keiper-Hrynko, T. Q. Shang, T. S. Ganzke, M. Toni, L. D. Valle, L. Alibardi, *J. Exp. Zool. B: Mol. Dev. Evol.* **2009**, *312B*, 58.
[24] L. Alibardi, *Tissue Cell* **2013**, *45*, 231.
[25] N. W. Rizzo, K. H. Gardner, D. J. Walls, N. M. Keiper-Hrynko, T. S. Ganzke, D. L. Hallahan, *J. R. Soc. Interface* **2006**, *3*, 441.
[26] Q. Xu, Y. Wan, T. S. Hu, T. X. Liu, D. Tao, P. H. Niewiarowski, Y. Tian, Y. Liu, L. Dai, Y. Yang, Z. Xia, *Nat. Commun.* **2015**, *6*, 8949.
[27] G. Huber, S. Orso, R. Spolenak, U. G. K. Wegst, S. Enders, S. N. Gorb, E. Arzt, *Mater. Res.* **2008**, *99*, 1113.
[28] M. Prowse, M. Wilkinson, J. Puthoff, G. Mayer, K. Autumn, *Acta Biomater.* **2010**, *7*, 733.
[29] X. Dong, R. Zhang, Y. Tian, M. A. Ramos, T. S. Hu, Z. Wang, H. Zhao, L. Zhang, Y. Wan, Z. Xia, Q. Xu, *ACS Appl. Polym. Mater.* **2020**, *2*, 2658.
[30] S. Páll, B. Hess, *Comput. Phys. Commun.* **2013**, *184*, 2641.
[31] D. van der Spoel, P. J. van Maaren, *J. Chem. Theory Comput.* **2006**, *2*, 1.
[32] H. J. C. Berendsen, J. P. M. Postma, W. F. van Gunsteren, A. DiNola, J. R. Haak, *J. Chem. Phys.* **1984**, *81*, 3684.
[33] G. Bussi, D. Donadio, M. Parrinello, *J. Chem. Phys.* **2007**, *126*, 014101.
[34] N. Goga, A. J. Rzepiela, A. H. de Vries, S. J. Marrink, H. J. C. Berendsen, *J. Chem. Theory Comput.* **2012**, *8*, 3637.
[35] B. N. J. Persson, S. Gorb, *J. Chem. Phys.* **2003**, *119*, 11437.
[36] E. Arzt, S. Gorb, R. Spolenak, *Proc. Natl. Acad. Sci. U.S.A.* **2003**, *100*, 10603.
[37] G. Huber, S. N. Gorb, R. Spolenak, E. Arzt, *Biol. Lett.* **2005**, *1*, 2.
[38] H. Grubmüller, *Methods Mol. Biol.* **2005**, *305*, 493.
[39] F. Rico, A. Russek, L. González, H. Grubmüller, S. Scheuring, *Proc. Natl. Acad. Sci. U.S.A.* **2019**, *116*, 6594.
[40] M. Varenberg, N. M. Pugno, S. N. Gorb, *Soft. Matter.* **2010**, *6*, 3269.
[41] A. R. C. Baljon, M. O. Robbins, *Science* **1996**, *271*, 482.
[42] A. Wang, S. Keten, *Npj. Comput. Mater.* **2019**, *5*, 1.
[43] G. Hummer, A. Szabo, *Proc. Natl. Acad. Sci. U.S.A.* **2001**, *98*, 3658.
[44] S. Sheridan, F. Gräter, C. Daday, *J. Phys. Chem. B* **2019**, *123*, 3658.
[45] F. J. Richards, *J. Exp. Bot.* **1959**, *10*, 290.